Brush border protocadherin CDHR2 promotes the elongation and maximized packing of microvilli in vivo

Julia A. Pinette, Suli Mao, Bryan A. Millis, Evan S. Krystofiak, James J. Faust, and Matthew J. Tyska*
Department of Cell and Developmental Biology, Vanderbilt University School of Medicine, Nashville, TN 37232

ABSTRACT Transporting epithelial cells optimize their morphology for solute uptake by building an apical specialization: a dense array of microvilli that serves to increase membrane surface area. In the intestinal tract, individual cells build thousands of microvilli, which pack tightly to form the brush border. Recent studies implicate adhesion molecule CDHR2 in the regulation of microvillar packing via the formation of adhesion complexes between the tips of adjacent protrusions. To gain insight on how CDHR2 contributes to brush border morphogenesis and enterocyte function under native in vivo conditions, we generated mice lacking CDHR2 expression in the intestinal tract. Although CDHR2 knockout (KO) mice are viable, body weight trends lower and careful examination of tissue, cell, and brush border morphology revealed several perturbations that likely contribute to reduced functional capacity of KO intestine. In the absence of CDHR2, microvilli are significantly shorter, and exhibit disordered packing and a 30% decrease in packing density. These structural perturbations are linked to decreased levels of key solute processing and transporting factors in the brush border. Thus, CDHR2 functions to elongate microvilli and maximize their numbers on the apical surface, which together serve to increase the functional capacity of enterocyte.

INTRODUCTION

Polarized epithelial cells like those that line the kidney tubules, intestinal tract, lung, or inner ear assemble apical specializations to enable specific physiological functions. In the case of intestinal epithelial cells, the apical domain is responsible for nutrient processing and uptake. To perform these functions efficiently, enterocytes assemble a brush border: a dense array of finger-like membrane protrusions known as microvilli (Crawley et al., 2014a; Delacour et al., 2016). Supported by a single parallel actin bundle composed of 20–30 filaments, each microvillus is cylindrical in shape and extends a micron or more from the cell surface into the gut lumen. Intestinal brush border microvilli are also remarkably uniform in diameter (~100 nm) and length (1–2 µm), and are tightly packed into highly ordered arrays such that a single enterocyte presents up to ~2000 protrusions. The molecular mechanisms that control microvillar dimensions, numbers, and packing density are of interest because these parameters ultimately dictate the holding capacity for membrane on the apical surface, and thus the functional capacity of the cell.

A growing literature suggests that one mechanism for organizing apical specializations involves physical adhesion between neighboring protrusions. In the enterocyte, two brush border–specific protocadherins, CDHR2 (also known as PCLKC and protocadherin-24) and CDHR5 (also known as mucin-like protocadherin and µ-protocadherin), form heterophilic complexes that link microvillar tips (Crawley et al., 2014b). CDHR2 can also form weak homophilic complexes, although the precise roles of the two different forms of adhesion are not known. Moreover, the cytoplasmic tails of both

Abbreviations used: ANKS4B, ankyrin repeat and sterile alpha motif domain containing 4B; CDH23, cadherin-23; CDHR2, cadherin related family member-2; CDHR5, cadherin related family member-5; DPPIV, dipeptidyl peptidase-IV; EGTA, ethylene glycol-bis(β-aminoethyl ether)-N,N,N',N'-tetraacetic acid; EM, electron microscopy; EUCOMM, European Conditional Mouse Mutagenesis Program; FFT, fast Fourier transform; H&E, hematoxylin and eosin; IAP, intestinal alkaline phosphatase; IMAC, intermicrovillar adhesion complex; KO, knockout; MYO7A, myosin-7A; MYO7B, myosin-7B; NHE3, sodium/hydrogen exchanger 3; PBS, phosphate-buffered saline; PCDH15, protocadherin related-15; PDZ, protein interaction motif with similarity to PSD95, DLG1, and ZO-1; RT, room temperature; SANS, scaffold protein containing ankyrin repeats and SAM domain; SEM, scanning electron microscopy; SI, sucrase-isomaltase; TEM, transmission electron microscopy; USH1C, USH1 protein network component harmonin; WT, wild type.

CDHR2 and CDHR5 interact with the PDZ domain protein USH1C and the actin-based motor MYO7B, which along with ankyrin repeat protein ANKS4B, serve to enrich adhesion complexes at the distal tips of microvilli (Crawley et al., 2014b; Li et al., 2016, 2017; Weck et al., 2016; Yu et al., 2017). Collectively, the two brush border protocadherins along with their three cytoplasmic binding partners are referred to as the intermicrovillar adhesion complex (IMAC). Knockdown (KD) of CDHR2 or its interactors CDHR5, MYO7B, or ANKS4B in the CACO-2$_{BBE}$ intestinal epithelial cell culture model leads to general brush border disarray (Crawley et al., 2014b; Weck et al., 2016), suggesting an important role for the IMAC in microvillar organization; knockout (KO) of USH1C in mice leads to similar phenotypes (Crawley et al., 2014b).

An IMAC-like complex is also found in the inner ear, where adhesion links form between adjacent stereocilia and play important roles in controlling the organization of stereocilia during hair cell morphogenesis, as well as mechanosensory function in mature hair cells (Schwander et al., 2010). The tip-link is a heterophilic adhesion complex formed from CDH23 (phylogenetically related to CDHR2) and PCDH15 (phylogenetically related to CDHR5; Siemens et al., 2004; Ahmed et al., 2006; Kazmierczak et al., 2007). CDH23 links to the actin cytoskeleton in taller stereocilia through a tripartite complex composed of SANS, USH1C, and MYO7A (Boeda et al., 2002; Siemens et al., 2002; Weil et al., 2003; Adato et al., 2005; Senften et al., 2006; Pan et al., 2009; Bahloul et al., 2010; Yan et al., 2010; Grati and Kachar 2011; Yu et al., 2017). The opposite end of the tip-link containing PCDH15 connects to the tips of shorter stereocilia, where it interacts with a mechanotransduction channel at least partially composed of TMC1 (Pan et al., 2018). The functional importance of the tip-link is underscored by the fact that loss-of-function mutations in any complex component lead to type 1 Usher syndrome, the leading cause of inherited deaf-blindness (Lentz and Keats, 1993). USH1C is expressed in the gut and inner ear and is therefore a shared component of both cytoplasmic tripartite complexes. Consequently, Usher syndrome patients with perturbations in USH1C present with gastrointestinal symptoms in addition to sensory dysfunction (Bitner-Glindzicz et al., 2000; Verpy et al., 2000). Notably, apical adhesion complexes like those found in the gut and inner ear are evolutionarily ancient, appearing in the earliest eukaryotes with simple transporting epithelial structures (Pena et al., 2016).

Previous studies in CACO-2$_{BBE}$ cells suggest that tip-localized adhesion links play an important role in the ordered packing of microvilli, which we expect to be critical for maximizing enterocyte function (Crawley et al., 2014b). Based on published data, both forms of intermicrovillar adhesion (homophilic and heterophilic) are expected to require CDHR2. CDHR2 is most highly expressed in small intestine but is also found in other epithelial tissues including colon, liver, testis, and kidney. As a nonclustered protocadherin, CDHR2 is a 1310 amino acid (a.a.) (~141 kDa) type I transmembrane protein consisting of an N-terminal ectodomain with nine tandem extracellular cadherin (EC) repeats that mediate adhesion, a central single-pass transmembrane domain, and a C-terminal cytoplasmic domain that mediates interactions with binding partners. Although the most N-terminal EC domain is required for CDHR2 function (Crawley et al., 2014b), mechanisms of homophilic and heterophilic adhesion have not been elucidated at a structural level. CDHR2 has also been identified as a potential tumor suppressor in colon and liver cancers (Okazaki et al., 2002), and may play a role in contact inhibition in HCT116 colon carcinoma cells (Ose et al., 2009, 2012). Additionally, CDHR2 may be a target of proteases secreted by attaching/effacing pathogens during infection (In et al., 2016). Most recently, loss of CDHR2 and IMAC component expression was linked to perturbations in brush border structure observed in Crohn's disease patients (VanDussen et al., 2018).

To test the hypothesis that CDHR2-dependent intermicrovillar adhesion and tight packing of microvilli are essential for normal enterocyte and intestinal function, we developed a mouse model lacking CDHR2 expression in the intestinal tract. CDHR2 KO mice trend smaller than their wild-type littermates, and careful examination at the tissue, cell, and subcellular levels revealed several new insights on how CDHR2 contributes to normal intestinal physiology. Strikingly, loss of CDHR2 gave rise to significant perturbations in microvillar morphology and packing organization, reducing overall packing density by ~30%. These and other structural defects were linked to decreased levels of key apical enzymes and transporters, which offer a mechanistic explanation for the reduced body weight of these animals. Together these studies suggest that CDHR2 contributes to enterocyte and intestinal function by optimizing brush border morphology for peak functional capacity.

RESULTS

CDHR2 KO mice are viable but exhibit reduced body weight

Mice harboring a CDHR2^{tm1a} allele were developed in-house using ES cells acquired from EUCOMM (Friedel et al., 2007). Following successful germline transmission, we created a conditional allele (CDHR2^{tm1c}) to eliminate potential interference from the tm1a cassette (Figure 1A; see also Supplemental Figure 1). CDHR2$^{tm1c/+}$ animals were then crossed with villin-CRE mice (el Marjou et al., 2004) to create villin-CRE;CDHR2$^{tm1c/tm1c}$ animals. The genotype in villin-expressing tissues becomes CDHR2$^{tm1d/tm1d}$, which is nonexpressing and referred to as "CDHR2 KO" or "KO" herein (Figure 1A). Deletion of the critical exons in CDHR2$^{tm1d/tm1d}$ mice was validated using PCR (Figure 1, A and B), and Western blotting was used to confirm loss of protein expression (Figure 1C); no bands of smaller molecular weight were detected using antibodies that recognized juxtamembrane regions of the CDHR2 ectodomain. Although CDHR2 KO pups initially exhibited similar body weight when compared with wild-type (WT) littermates, growth began to lag behind that of WT animals in the second month of life into adulthood (Figure 1, D and E). No other overt symptoms, anomalous behaviors, or health issues were noted in CDHR2 KO animals. Examination of hematoxylin and eosin (H&E) stained Swiss roll sections revealed some perturbations to epithelial architecture in CDHR2 KO mice (Figure 1F). Although we found no significant differences in gut length, mean villus length and crypt depth measured at the proximal (duodenal) end of the small intestine were significantly decreased (Figure 1, G and H).

Enterocyte morphology is perturbed in CDHR2 KO mice

To examine CDHR2 KO tissue morphology, we first fixed samples for scanning electron microscopy (SEM). At low magnifications (Figure 2A, i and ii), KO tissue segments looked generally similar to WT samples, although some KO samples exhibited bare zones in the epithelium that lacked closely spaced villi (see yellow asterisks in Figure 2A, KO ii). Notably, higher-magnification images of CDHR2 KO samples revealed villus surfaces that were rougher and less flat in appearance (Figure 2A, KO iii). To more specifically examine brush border and enterocyte morphology, CDHR2 KO tissue sections were stained with phalloidin or villin to highlight the apical brush border, and E-cadherin to delineate cell margins; samples were then subject to confocal microscopy. Phalloidin and villin staining showed that CDHR2 KO villus epithelial cells exhibit a clear enrichment of apical signal that corresponds to the brush border (Figure 2, B–D). However, as alluded to above, we also noted that
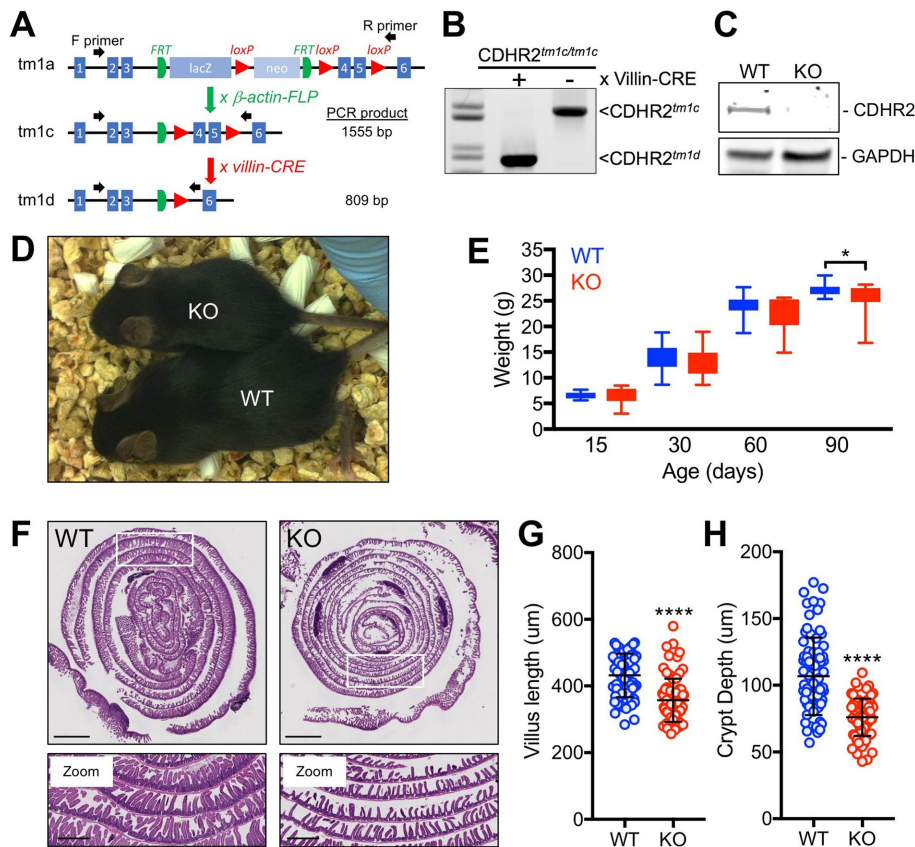
FIGURE 1: CDHR2 KO mice exhibit growth defects. (A) Cartoon of the strategy used to generate the tm1d CDHR2 KO allele from tm1a mice. Binding sites of forward and reverse primers used to genotype these animals are shown with black arrows. Expected PCR band sizes for the tm1c and tm1d alleles are also given. (B) PCR genotyping confirmation of the allele conversion to CDHR2^{tm1d} upon crossing CDHR2^{tm1c} animals with mice harboring villin-CRE. (C) Western blotting validation of loss of CDHR2 expression in the isolated intestinal epithelium of CDHR2^{tm1d}/CDHR2^{tm1d} mice. (D) Photograph of WT and CDHR2 KO littermates at P30. (E) Comparison of male WT and CDHR2 KO littermate body weights at P15 (WT, $n = 9$, 6.6 ± 0.7 g; KO, $n = 9$, 6.4 ± 1.7 g), P30 (WT, $n = 20$, 14.0 ± 2.6 g; KO, $n = 20$, 13.2 ± 2.9 g), P60 (WT, $n = 13$, 24.0 ± 2.3 g; KO, $n = 9$, 22.4 ± 3.5 g), and P90 (WT, $n = 14$, 27.2 ± 1.3 g; KO, $n = 28$, 25.2 ± 3.3 g). Values are mean $\pm$ SD, P90, *$p < 0.05$. Whiskers on box plots indicate min/max values. (F) H&E-stained Swiss roll sections of paraffin-embedded small intestine from WT and CDHR2 KO mice. Scale bars are 2 mm for whole Swiss roll and 500 μm for zoom panels. (G) Quantification of villus length in WT and CDHR2 KO Swiss roll sections. WT, $n = 75$ measurements (25/Swiss roll, 1 Swiss roll/mouse, three mice), 431 ± 65 μm; KO, $n = 7$; (25/Swiss roll, 1 Swiss roll/mouse, three mice), 357 ± 65 μm. Values indicate mean $\pm$ SD; ****, $p < 0.0001$. (H) Quantification of crypt depth in WT and CDHR2 KO Swiss roll sections. WT, $n = 75$ measurements (25/Swiss roll, 1 Swiss roll/mouse, three mice), 107 ± 29 μm; KO, $n = 75$ measurements (25/Swiss roll, 1 Swiss roll/mouse, three mice), 82 ± 11 μm. Values indicate mean $\pm$ SD; ****, $p < 0.0001$.

CDHR5, USH1C, and MYO7B from the brush border and significantly lower levels in whole cell lysates (Weck et al., 2016). To determine the impact of CDHR2 KO on other IMAC components in vivo, we stained small intestinal tissue paraffin-embedded sections with antibodies directed against CDHR5, USH1C, and MYO7B, and imaged stained sections using confocal microscopy (Figure 3). In the case of cytoplasmic components USH1C and MYO7B, inspection of low-magnification images revealed notable increases in cytoplasmic signal (Figure 3, A and B), consistent with some loss from the brush border. In all three cases, however, signal remained in the brush border, but the enrichment normally observed at the distal tips of microvilli was lost in CDHR2 KO tissue samples (Figure 3, A–C, white arrows in WT zoom panels). Thus, in the absence of membrane-associated CDHR2 other IMAC components are unable to maintain their normal localization at the tips of microvilli.

Microvillar ultrastructure is disrupted in the absence of CDHR2

To further develop our understanding of how loss of CDHR2 function impacts microvillar ultrastructure and organization, we prepared CDHR2 KO samples for transmission electron microscopy (TEM). TEM of the brush borders in jejunal tissues revealed that KO enterocytes exhibit prominent apical "doming" (Figure 4A) as alluded to above. However, we also observed CDHR2 KO microvilli are significantly shorter and more variable in length, lacking the uniformity that is characteristic of the intestinal brush border (Figure 4, A and B; 1084 ± 110 nm vs. 682 ± 180 nm, mean $\pm$ SD). Thus, under normal conditions CDHR2 promotes the elongation of brush border microvilli to a common length. CDHR2 KO microvilli also exhibited a splayed morphology with significant physical separation and free space between neighboring protrusions (Figure 4A, KO zoom panel). Notably, when viewed from this perspective, the intermicrovillar adhesion links normally visualized at the tips of WT microvilli (Figure 4A, black arrows in WT zoom panel) were almost entirely absent in KO brush borders, which supports the role of CHDR2 in adhesion link formation in vivo. However, in rare cases, we were able to observe remnant link-like structures between some microvilli when viewed in cross-section (Figure 4C, yellow arrows in KO zoom panel).

KO villus epithelial surfaces appeared less flat than WT, with individual enterocytes presenting a "domed" apical surface characterized by abnormal outward/convex curvature (Figure 2C). Despite these perturbations to cell shape, E-cadherin staining showed that KO enterocytes maintained apical–basolateral polarity and simple columnar morphology (Figure 2D).

IMAC components are displaced from the tips of microvilli in the absence of CDHR2

Previous studies of an USH1C KO mouse revealed that other IMAC components CDHR5, ANKS4B, and MYO7B were no longer enriched at microvillar tips in the absence of this protein scaffold (Crawley et al., 2014b; Weck et al., 2016). Studies in CACO-2$_{BBE}$ cells also showed that ANKS4B KD resulted in loss of CDHR2,

Microvillar packing is disrupted in the absence of CDHR2

Next, we imaged regions of TEM sections that offered views of microvillar cross-sections. Owing to their cylindrical shape, microvilli in cross-section typically appear as ~100-nm-diameter rings, with an outer electron density representing the plasma membrane and an inner density corresponding to actin filaments in the core bundle. Strikingly, microvillar cross-sections in CDHR2 KO samples were no
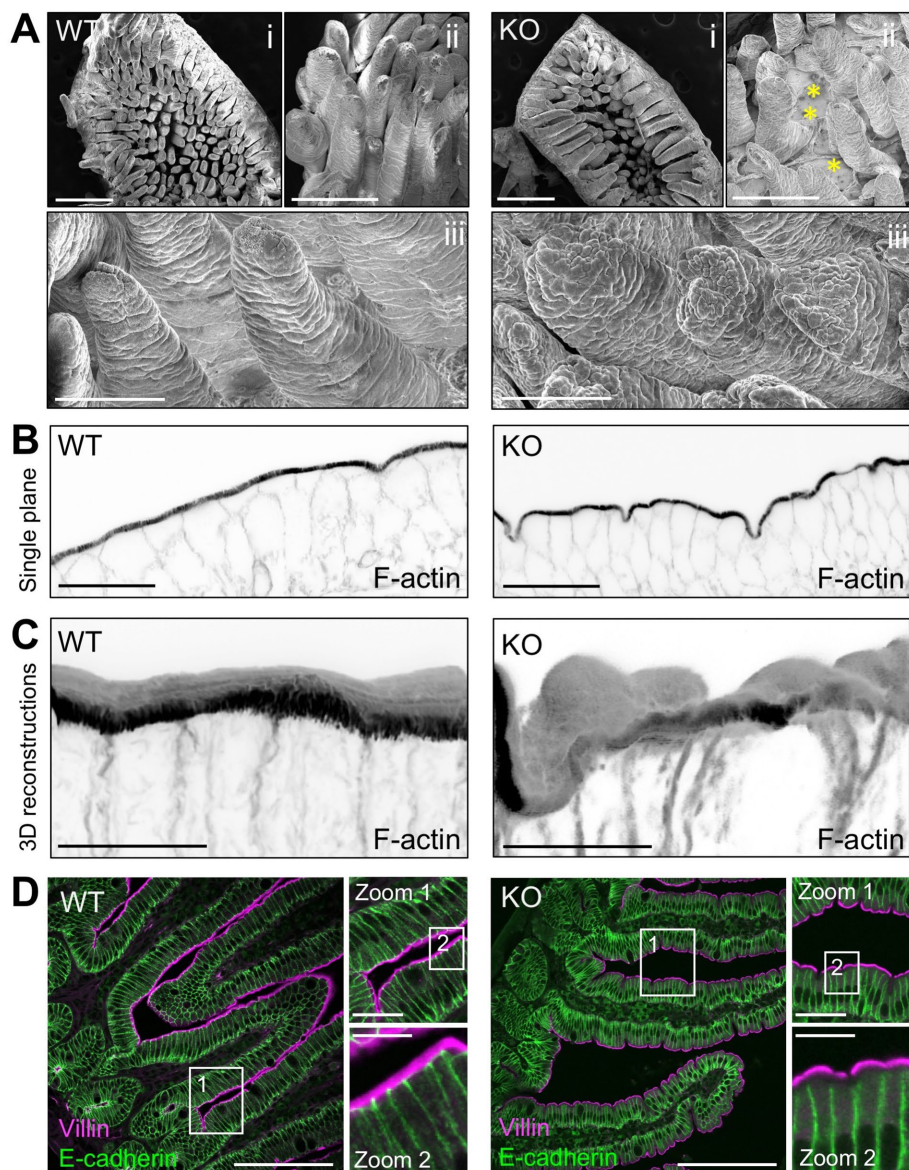
FIGURE 2: CDHR2 KO mice exhibit perturbations in the intestinal epithelium. (A) SEM images for intestinal tissue samples from WT and CDHR2 KO mice. Scale bars are 500 μm for Ai, 200 μm for Aii, 100 μm for Aiii; yellow asterisks in KO Aii indicate a large region of the epithelium lacking villi. (B) Single image planes of Alexa488-phalloidin–stained frozen tissue sections from WT and CDHR2 KO mice, acquired with a laser-scanning confocal microscope. Signal is inverted to facilitate visualization. Scale bars are 25 μm. (C) Three-dimensional reconstructions (8 μm thick) of deconvolved laser-scanning confocal volumes from the WT and CDHR2 KO samples imaged in B. Signal is inverted to facilitate visualization. Scale bars are 10 μm. (D) Single confocal image planes of WT and CDHR2 KO tissue sections stained with anti-villin (green) to highlight the brush border and anti–E-cadherin (magenta) to label cell margins. Zoom 1 shows the region in the main panel highlighted by the small white box; zoom 2 shows the region in zoom 1 highlighted by the small white box. Scale bars are 100 μm for main panels, 25 μm for zoom 1, and 10 μm for zoom 2.

sections revealed a significant increase (Figure 4E). We also noted that misshapen KO microvilli harbored abnormally large, poorly consolidated core actin bundles or in some cases multiple core-like structures (Figure 4C, white arrowheads on KO zoom panel). Thus, CDHR2 constrains the diameter of microvilli and promotes the maintenance of their stereotypical cylindrical shape under normal conditions.

In TEM cross-sections, we also observed that KO microvilli were typically separated by abnormally large regions of free space (Figure 4C, KO), suggesting reduced packing density in KO brush borders. To more closely examine microvillar packing order and density in KO samples, we returned to a SEM approach. We examined the packing order of microvilli in SEM images by performing fast Fourier transforms (FFTs) of square regions of apical surface corresponding roughly to the area of a single cell. For WT samples, the resulting frequency domain images contained six robust first-order peaks in the expected hexagonal pattern (Figure 5A, WT inset). FFTs of CDHR2 KO images lacked clear first-order peaks and instead contained a ring-shaped pattern indicating the less organized liquid packing of microvilli (Figure 5A, KO inset). CDHR2 KO brush borders also presented fewer microvilli per unit apical area (Figure 5, B–D). Calculating the average nearest-neighbor distance for WT microvilli revealed a spacing of 93.5 ± 14.1 nm (center-center, mean ± SD), whereas KO spacing was significantly increased at 111.4 ± 13.9 nm (Figure 5, C and D). This modest increase in spacing gave rise to a marked reduction in microvillar packing density, with CDHR2 KO enterocytes presenting ~33% fewer protrusions per unit apical area (81.8 microvilli/μm^2 in WT vs. 55.0 microvilli/μm^2 in KO). Together, these results show that CDHR2 is essential for generating the maximally packed hexagonal arrays of microvilli that are characteristic of the enterocyte brush border.

Levels of apical enzymes and transporters are reduced in the absence of CDHR2

Our confocal and ultrastructural analyses indicate that the loss of CDHR2 results in shorter microvilli that are reduced in number per unit apical area. Together, these perturbations should limit the apical plasma membrane scaffolding capacity of CDHR2 KO enterocytes. If this is the case, one would expect apical levels of membrane-associated enzymes and structural components to be reduced in KO samples. To test this prediction, we stained WT and CDHR2 KO tissue sections for integral membrane proteins including intestinal alkaline phosphatase (IAP), sucrase-isomaltase (SI), dipeptidyl peptidase-IV

longer circular and instead exhibited more angular or oblong profiles (Figure 4C), which we quantified by calculating a "circularity" metric (Figure 4D; perfect circles exhibit a circularity of 1, less circular objects <1). Although some of these noncircular profiles may be related to the splaying of protrusions observed in lateral views of the brush border (Figure 4A), other cross-sections were distorted in ways that cannot be explained by splaying (Figure 4C, KO montage at right). Moreover, quantification of the area occupied by KO cross-
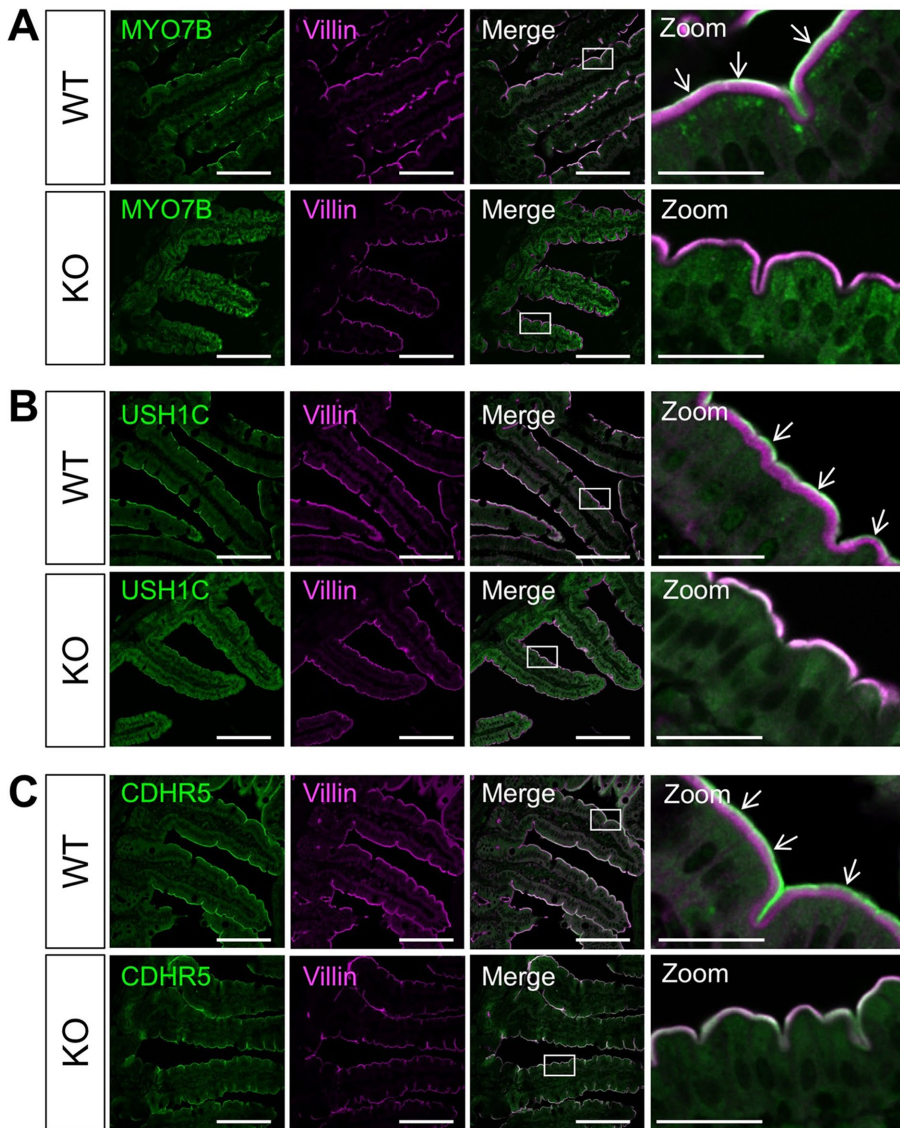
FIGURE 3: IMAC components are mislocalized in CDHR2 KO brush borders. Single confocal image planes of WT and CDHR2 KO paraffin-embedded tissue sections stained with anti-villin (magenta) to highlight the brush border and (A) anti-MYO7B (green), (B) anti-USH1C (green), or (C) anti-CDHR5 (green). Scale bars are 100 μm for main panels and 25 μm for zoom panels. Zoom panels show the region in the main merge panel highlighted by the small white box.

(Crawley *et al.*, 2014b). SEM images of CDHR2 KD cells revealed "disheveled" brush borders with poorly organized microvilli, which also appeared to exhibit much greater variability in length. Here, we extend these initial findings by examining the impact of CDHR2 KO in a newly developed mouse model. Given the exquisite organization of the brush border and highly ordered packing of microvilli presented by normal native intestinal tissues, we expected that even subtle effects on microvillar structure and organization would be resolved in CDHR2 KO tissues. Indeed, we found that microvillus length, shape, and packing are all impacted by CDHR2 KO. This has consequences for membrane scaffolding at the apical surface, as CDHR2 KO brush borders fail to enrich high levels of the membrane-associated transporters that are critical for enterocyte function. We propose that the observed reduction in key apical transporters and enzymes impairs nutrient uptake, and this in turn provides a molecular underpinning for the growth defects observed at the whole animal level.

Examination of CDHR2 KO tissues revealed several interesting insights on CDHR2 function under normal conditions. At the cellular level, we observed that the apical domains of CDHR2 KO enterocytes exhibit a striking "domed" appearance with marked outward curvature (Figure 2). Bulging brush borders might indicate an attempt by the enterocyte to compensate for the loss of functional microvilli (more below) by overproducing and delivering excess material to the apical domain. If this is the case, our results would argue that CDHR2 normally functions to oppose other factors known to drive apical expansion, such as Dbl3, an ezrin-interacting activator of CDC42 (Zihni *et al.*, 2014). Yet this interpretation is not supported by our apical marker analysis (Figure 6), which argues that despite their domed appearance, overall levels of key apical factors are significantly reduced in CDHR2 KO tissues. A second more likely explanation is that apical doming simply represents the mechanical consequence of eliminating adhesion between microvillar tips, which normally serves to force the tips into a single plane and promote the flatness of the apical surface. Although speculative, flattening may help reduce or prevent damage of the apical surface in response to flow of luminal contents or peristaltic contractions that are continuously experienced by the intestinal epithelium.

We also observed that KO microvilli are abnormally short (Figure 4), suggesting that CDHR2 serves to elongate these protrusions. The idea that CDHR2 promotes microvillar elongation is consistent with previous studies showing that overexpression of EGFP-CDHR2 increases apical F-actin signal as visualized with phalloidin (Crawley *et al.*, 2014b). How CDHR2 promotes microvillar elongation remains unclear, but this factor does localize to the distal tips, where the

(DPPIV), and sodium/hydrogen exchanger 3 (NHE3), as well as the peripheral membrane protein ezrin, and imaged samples using identical settings on the confocal microscope to allow for quantitative analysis of fluorescence intensities. Strikingly, all of these membrane-associated apical markers demonstrated significantly reduced levels in the brush border (Figure 6). In particular, levels of SI, DPPIV, and NHE3 were dramatically lower in KO samples, which exhibited an almost complete absence of the intense band of signal normally observed at the apical surface. Thus, reduced microvillar length and packing density are linked to a decreased capacity for scaffolding membrane-associated proteins in CDHR2 KO brush borders.

DISCUSSION

The initial perturbation studies implicating CDHR2 in brush border assembly took advantage of short hairpin RNA knockdown to reduce its levels in the CACO-2$_{BBE}$ intestinal epithelial cell line
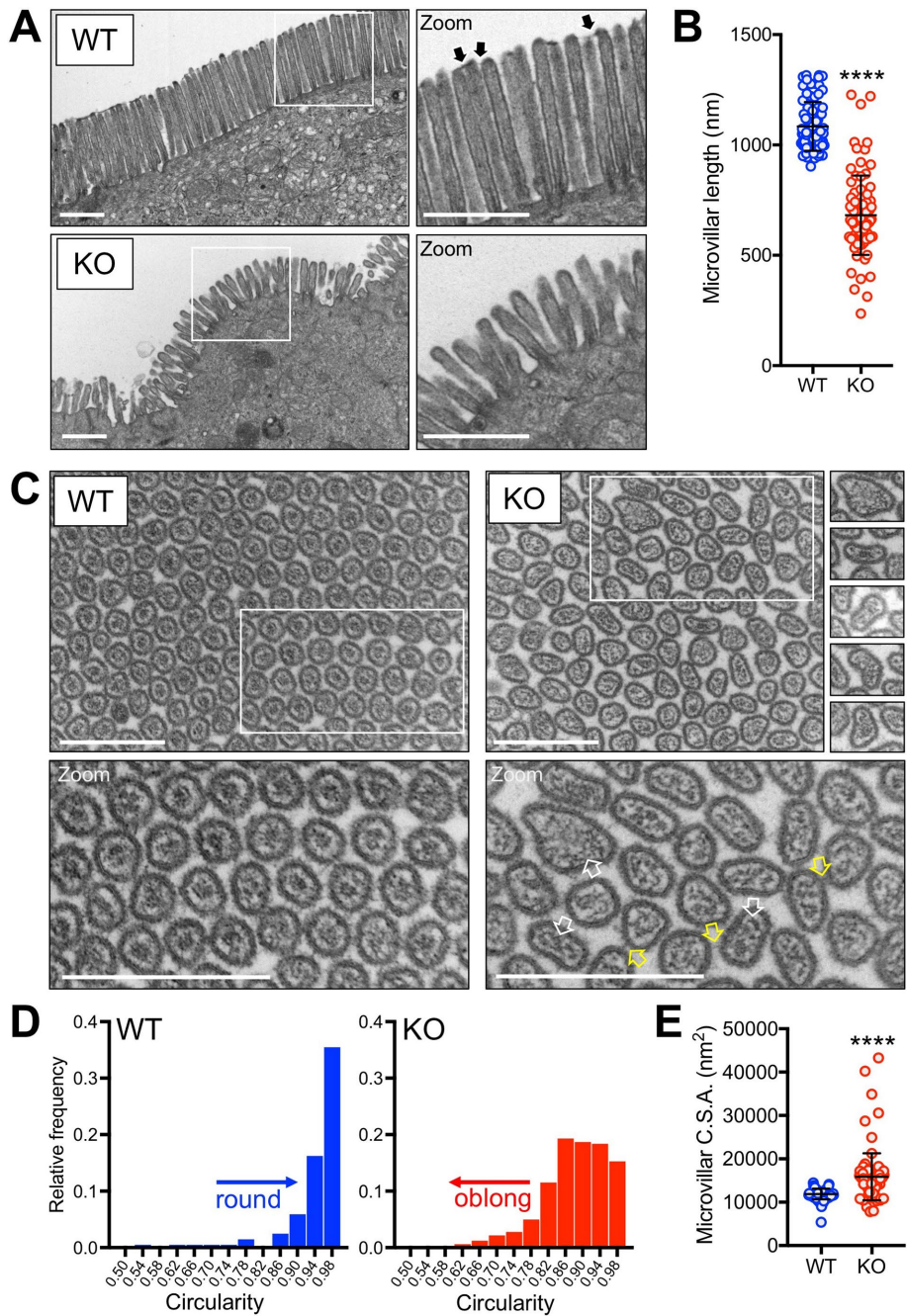
FIGURE 4: Microvillar ultrastructure is perturbed in CDHR2 KO brush borders. (A) TEM images of WT and KO brush borders in a plane parallel to the microvillar axis; white dashed boxes show regions highlighted in zoom panels to the right. Black arrows in WT zoom panel highlight intermicrovillar adhesion links at the distal tips of microvilli. (B) Quantification of microvillar length in WT and KO brush borders. WT, $n = 85$ measurements, 1084 ± 110 nm; KO, $n = 82$ measurements, 682 ± 180 nm. Values indicate mean $\pm$ SD; ****, $p < 0.0001$. Length measurements were highly selective such that only protrusions with actin cores that are clearly visible along their full length were scored. (C) TEM images of WT and KO brush borders in a plane perpendicular to the microvillar axis; white boxes show region highlighted in zoom panels below. Image montage to the right of the KO panel shows several examples of distorted microvillus cross-sections. White outlined arrows in the KO zoom panel highlight a subset of the poorly consolidated and misshapen core actin bundles. Yellow outlined arrows in the KO zoom panel highlight remnant intermicrovillar link-like structures. (D) Frequency distributions of circularity measurements on microvillar cross-sections, where perfect circles exhibit a circularity of 1, less circular objects <1 ($n = 203$ cross-sections for WT and $n = 321$ for KO). (E) Quantification of microvillar cross–sectional area. WT, $n = 98$ cross-sections, $11,895 \pm 1227$ nm^2; KO, $n = 98$, $15,872 \pm 5394$ nm^2. Values indicate mean $\pm$ SD; ****, $p < 0.0001$. All scale bars **are** 500 nm.

barbed ends of actin filaments that comprise the core bundle are found. Because the barbed ends are the preferred site for incorporation of new actin monomers, one possibility is that the CDHR2 cytoplasmic domain or its binding partners promote actin incorporation directly at these sites. At present, the only known actin-binding CDHR2 interactor is the MyTH4/FERM domain-containing myosin, MYO7B, which normally accumulates at microvillar tips (Weck et al., 2016), but is lost from CDHR2 KO brush borders (Figure 3). Interestingly, *Dictyostelium* myosin-7 has been implicated in filopod initiation and elongation (Tuxworth et al., 2001; Petersen et al., 2016). Another MyTH4/FERM myosin, myosin-10, also targets to the tips of filopodia where it promotes their growth by delivering cargoes that promote elongation (Berg and Cheney 2002; Tokuo and Ikebe 2004; Zhang et al., 2004; Bohil et al., 2006). In a similar manner, MYO7B might serve to deliver an as-of-yet unidentified cargo to microvillar tips, which in turn serves to lengthen these structures.

One unexpected finding was that a subset of CDHR2 KO microvilli exhibit irregular noncylindrical shapes that result in noncircular TEM cross-sections (Figure 4). These defects in microvillar shape were also coupled to perturbations in the supporting core actin bundles; KO microvilli contained large core-like structures that filled the expanded cross-sectional areas of these protrusions. Although it remains unclear why loss CDHR2 leads to a loss of cylindrical shape, this finding provokes some new ideas on factors that shape these protrusions. For example, under normal conditions, a single microvillus tip interacts directly with surrounding adjacent microvilli through 15–20 adhesion links (Crawley et al., 2014b), which are at least in part composed of CDHR2. This radial arrangement of extracellular adhesion links creates, on the inside of the cell, a corresponding radial array of CDHR2 cytoplasmic domains, which serve as docking sites for the cytoplasmic IMAC components, ANKS4B, USH1C, and MYO7B. Together, these factors likely play a role in "pinning" the apical plasma membrane to the underlying core actin bundle. We speculate that loss of these radially arranged pinning forces in CDHR2 KO enterocytes may be responsible for the aberrant, noncylindrical microvilli observed in mutant brush borders.

CDHR2 KO microvilli exhibit a striking loss of hexagonal packing order and significantly lower packing densities (Figure 5), results consistent with the CDHR2 KD phenotype in CACO-2$_{BBE}$ cells (Crawley et al., 2014b). In jejunal intestinal tissues,
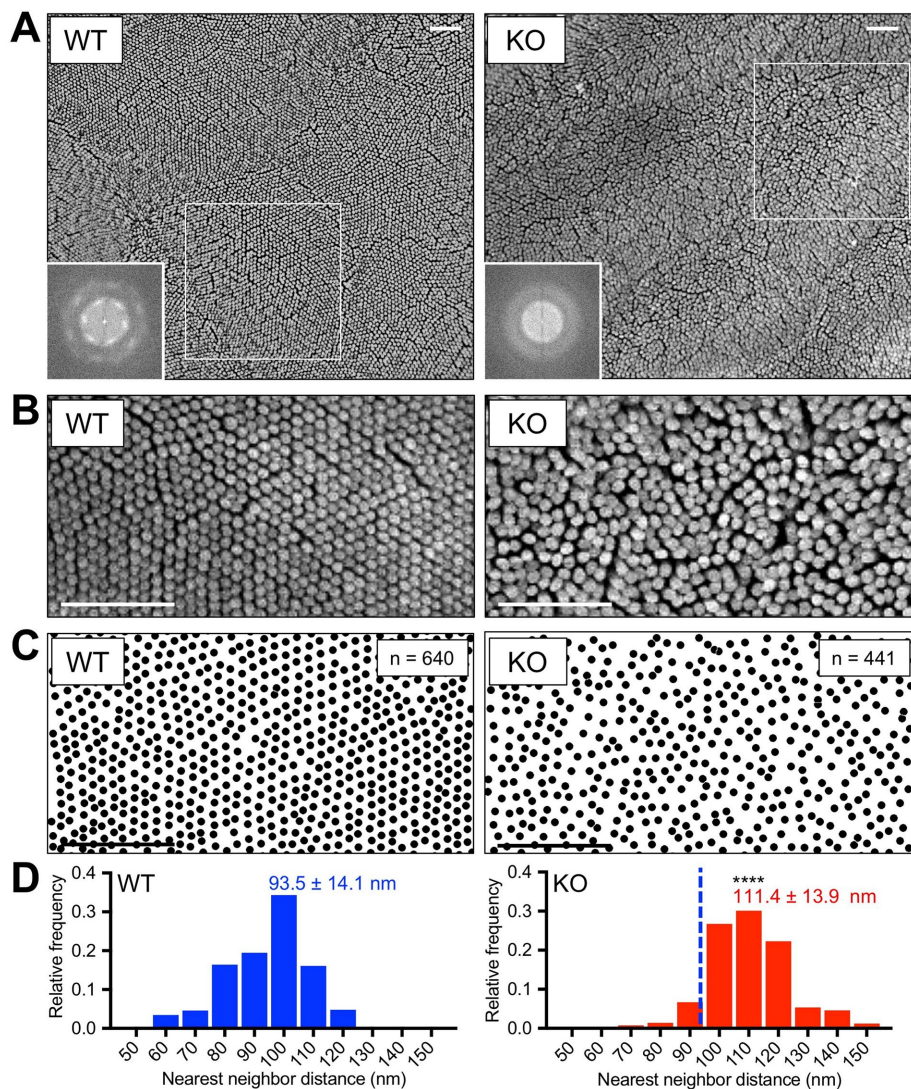
FIGURE 5: Microvillar packing density is decreased in CDHR2 KO brush borders. (A) SEM images show en face views of microvilli in WT and KO brush borders at intermediate magnification. Insets in both panels show FFT frequency domain images calculated from the regions highlighted by the white boxes. (B) High-magnification SEM images of microvilli in WT and KO brush borders reveal packing defects in KO samples. (C) Black spots represent the positions of microvillar tips in the images shown in B. The number of microvilli counted in each field is shown in the upper right-hand corner. (D) Frequency distributions of the nearest-neighbor distance calculated for WT and CDHR2 KO microvilli. WT, $n = 24{,}036$ measurements, 93.5 ± 14.1 nm; KO, $n = 18{,}268$ measurements, 111.4 ± 13.9 nm. Values indicate mean $\pm$ SD; ****, $p < 0.0001$. Vertical dashed blue line on the KO plot indicates mean nearest-neighbor distance for WT. All scale bars are 1 µm.

Whereas CDHR2 KO markedly reduced the number of intermicrovillar adhesion links observed in our TEM images, link-like structures were still evident in some sections (Figure 4C, yellow arrows), suggesting that not all intermicrovillar links are CDHR2 dependent. Although we found that CDHR5 is still present in KO brush borders (Figure 3C), previous biochemical studies showed that this protocadherin is unable to form adhesion complexes without CDHR2 (Crawley *et al.*, 2014b). Although no other intermicrovillar adhesion factors have been identified to date, early studies proposed that carcinoembryonic antigen-related cell adhesion molecule 1 (also known as CEACAM1 or CD66a), a bona fide resident of the enterocyte brush border (McConnell *et al.*, 2011), might play such a role (Sundberg and Obrink, 2002). Future studies could take advantage of the CDHR2 KO mouse model to test this proposal or identify other factors that also contribute to intermicrovillar adhesion and packing order.

Our findings also lead to interesting questions about the relationship between microvillar growth and packing. The fact that CDHR2 KO packing density is reduced by ~30% suggests that intermicrovillar adhesion is needed for enterocytes to generate the high numbers of microvilli required for normal intestinal function. Although there is no direct evidence implicating CDHR2 in initiating microvillar growth per se, this study does implicate CDHR2 in protrusion elongation (Figure 4), which we expect to be critical for morphogenesis of microvilli following their emergence from the apical cell surface. Whether CDHR2 or other associated IMAC components contribute directly to the initiation of microvillar growth at the nascent apical membrane remains unclear. However, even in the absence of direct biochemical mechanisms, intermicrovillar adhesion could contribute indirectly to microvillar growth by sequestering existing microvilli and creating regions of free apical membrane that would in turn support the growth of new protrusions.

individual enterocytes are capable of presenting up to ~2000 hexagonally packed microvilli. Analysis of CDHR2 KO tissues revealed that distances between neighboring microvilli are increased and packing more irregular compared with WT samples (Figure 5). In CDHR2 KO brush borders, microvillar packing density is reduced ~30%, a decrease that was evident in both TEM images of microvillar cross-sections (Figure 4) as well as SEM images (Figure 5). These results indicate that a major function of CDHR2 is to maximize the number of microvilli per unit apical area by organizing these protrusions into hexagonal arrays. Defects in microvillar packing should be linked to a decreased capacity for scaffolding apical membrane and its associated transporters and channels, a prediction that we confirmed with apical marker analysis (Figure 6).

Future studies will need to examine the role of CDHR2 and its binding partners in microvillar growth and elongation.

Finally, we note that several of the phenotypes alluded to above are reminiscent of hair bundle defects reported in mice lacking functional CDH23 or PCDH15. Early in hair cell differentiation (embryonic day 18.5 [E18.5]), *CDH23* mutant mice exhibit abnormally short stereocilia precursors, while later stages (postnatal day 20 [P20]) are characterized by defects in the organization of stereocilia that do grow; these perturbations give rise to profound sensory dysfunction (Di Palma *et al.*, 2001; Holme and Steel 2002; Lefevre *et al.*, 2008). Loss of PCDH15 early in development also leads to defects in stereocilia formation and organization as early as P0 (Pawlowski *et al.*, 2006; Lefevre *et al.*, 2008). When combined with the defects in the
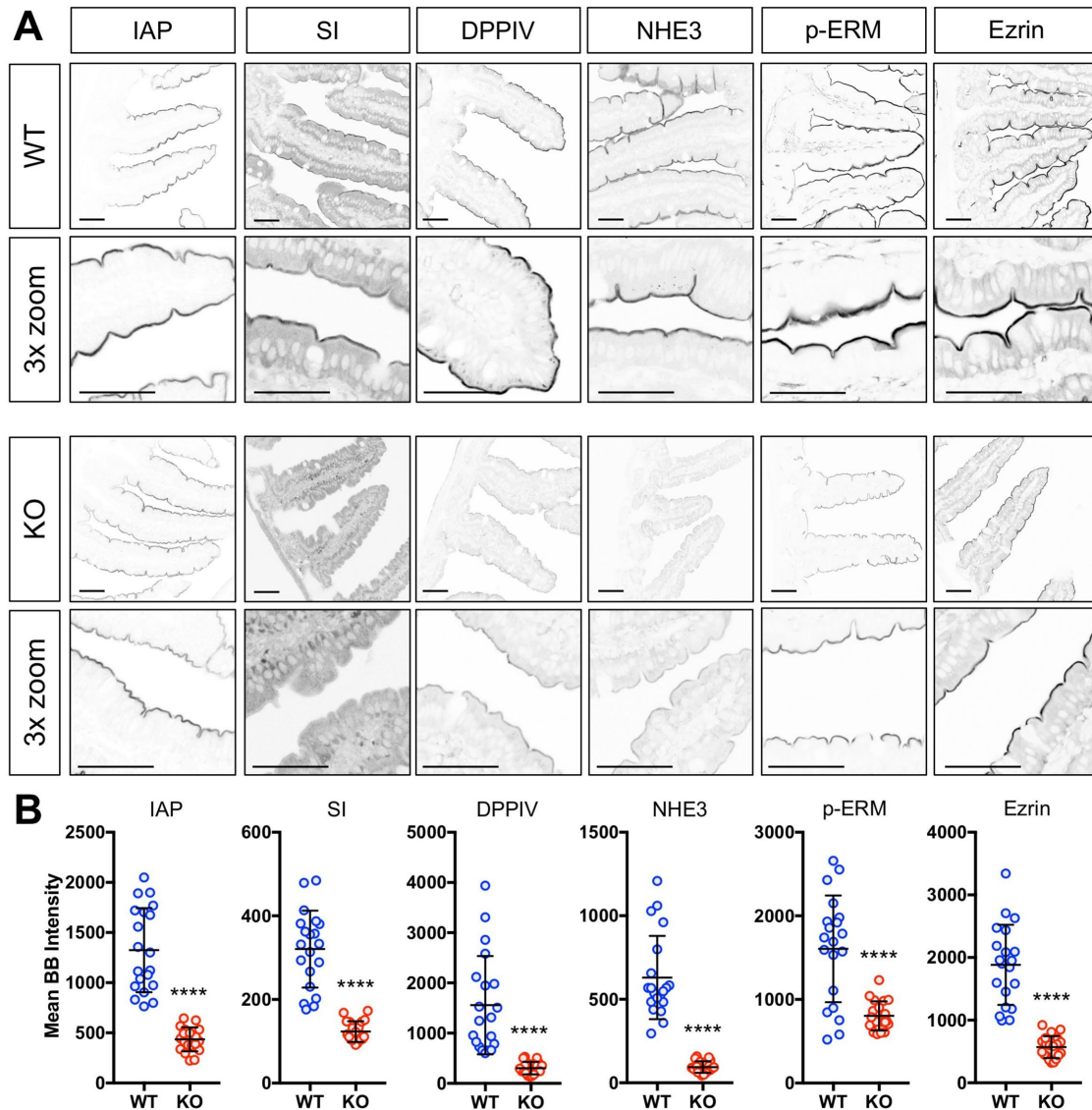
FIGURE 6: Levels of key apical markers are reduced in CDHR KO tissues. (A) Single confocal image planes of WT and CDHR2 KO paraffin tissue sections stained with primary antibodies targeting the apical marker indicated at the top of each image column. Top row shows native 40× magnification; bottom row shows tissue sections at threefold higher magnification. LUTs were inverted to facilitate visualization of intensity differences between WT and CDHR2 KO samples. All scale bars are 50 µm. (B) Quantification 12-bit fluorescence intensities from the brush border of WT and CDHR2 KO samples. Each plot consists of 20 measurements from sections representing multiple animals of each genotype. IAP, WT: 1325 ± 420 vs. KO 435 ± 119; SI, WT: 321 ± 92 vs. KO 123 ± 25; DPPIV, WT: 1558 ± 997 vs. KO 304 ± 124; NHE3, WT: 630 ± 249 vs. KO 94 ± 35; p-ERM, WT: 1605 ± 638 vs. KO 803 ± 173; ezrin, WT: 1884 ± 639 vs. 570 ± 176. Units = 12-bit fluorescence intensity; all values indicate mean $\pm$ SD; ****, $p < 0.0001$.

CDHR2 KO mice reported here, our data suggest that elongation and organization of finger-like protrusions represent two core conserved functions of tip-targeted adhesion links. In future studies, it will be interesting to determine whether other activities associated with stereocilia tip-links, such as mechanosensory function, manifest in simple transporting epithelial tissues like the kidney and gut.

MATERIALS AND METHODS

Tissue preparation

Animal experiments were carried out in accordance with American Veterinary Medical Association and Vanderbilt University School of Medicine IACUC guidelines. For histological staining with H&E, paraffin sections were prepared from the small and large intestines. Briefly, segments of small intestine and colon were excised from WT and KO mice, washed with room temperature (RT) phosphate-buffered saline (PBS), rolled from distal to proximal end, and fixed in 10% Formalin. Tissue rolls were then embedded in paraffin, sectioned, and stained by the Research Histology core at the Vanderbilt University School of Medicine. To prepare frozen tissue samples, segments of WT and KO intestine were removed and flushed with cold PBS supplemented with 1.2 mM $CaCl_2$ and 1 mM $MgCl_2$ and fixed with 2% paraformaldehyde (PFA) for 15 min. After initial fixation, the tube was cut along its length and fixed for an additional 2 h in 2% PFA at RT with

gentle agitation. Samples were washed with PBS three times, sub-dissected, and then floated lumen-side down in 30% sucrose with 1% sodium azide at 4°C overnight. Specimens were then streaked through embedding medium before being oriented in a block filled with fresh embedding medium and snap-frozen in dry ice–cooled acetone. Samples were cut into 10-µm sections and mounted on slides for staining and confocal imaging.

Western blotting

To prepare villus-enriched epithelial samples for Western blotting and PCR analysis (see below), mouse intestinal tissue segments were first washed in ice-cold PBS and then opened lengthwise using a cannula. To isolate the intestinal epithelium, the luminal surface was gently scraped using the edge of a microscope slide. To prepare samples for Western blotting, scrapates were incubated in cold RIPA buffer (150 mM NaCl, 1.0% NP-40, 0.5% sodium deoxycholate, 0.1% SDS, 50 mM Tris, pH 8.0) containing 2 mM ATP, cOmplete ULTRA tablets (Roche), and 1 mM Pefabloc (Roche). The resulting lysates were clarified by centrifugation at $16,000 \times g$ for 20 min, and then diluted with Laemmli sample buffer and heated at 95°C for 5 min. Samples were loaded for equal total protein and separated on a 4–12% Nu-Page gradient gel (Invitrogen). Proteins were then transferred to nitrocellulose overnight at 25 V. Membranes were blocked for 1 h in 10% milk–PBS and then incubated with primary antibodies (anti-CDHR2; Sigma HPA012569 or anti-GAPDH; Cell Signaling #2118L) diluted in PBS containing 0.1% Tween-20 (PBS-T) overnight at 4°C. Membranes were washed and then incubated with donkey anti-rabbit 800 IRdye (0.01 ug/ml, 926-32213; Li-Cor) or donkey anti-mouse 800 IRdye (0.01 µg/ml, 926-32212; Li-Cor) for 30 min. Membranes were then washed and Western blot signals were imaged using a Li-Cor Odyssey infrared imaging system.

PCR genotyping

To prepare samples for PCR genotyping, villus-enriched epithelial fractions were incubated in Nuclei Lysis Solution (Promega #A7941) with EDTA and Proteinase K at 55°C for 1 h. Protein Precipitation Solution (Promega #A795A) was then added per the manufacturer's recommendation, and samples were vortexed for 20 s and incubated on ice for 5 min. Samples were then clarified with centrifugation at $25,000 \times g$ for 10 min and DNA precipitated by addition of isopropanol. DNA was pelleted by centrifugation at $25,000 \times g$ for 1 min, and pellets were washed several times in 70% ethanol. Washed pellets were resuspended in 50 ml TE buffer in preparation for PCR analysis. PCR was performed using MyTaq Red Mix (Bioline Bio-25043) per the manufacturer's guidelines, using forward (5′-GAGGCATCCAAAGGTGGGTGA-3′) and reverse (5′-TCAAACGCTGGGGTCATGTTG-3′) primers designed to detect and differentiate tm1c and tm1d alleles (see Figure 1A and Supplemental Figure 1). Thermal cycler parameters were 95°C for 3 min, 30× (95°C for 30 s, 60°C for 30 s, 72°C for 45 s), 72°C for 7 min, then 4°C hold. PCR products were separated on a 1% agarose gel and visualized with ethidium bromide using a Gel Doc EZ system (Bio-Rad).

Antibody staining

Paraffin-embedded tissue sections of WT and CDHR2 KO small and large intestinal Swiss rolls were deparaffinized using Histo-Clear solution (Fisher) and rehydrated in a descending graded ethanol series. Slides were then subject to an antigen retrieval step consisting of boiling for 1 h in a solution of 10 mM Tris (pH 9.0) and 0.5 mM ethylene glycol-bis(β-aminoethyl ether)-N,N,N′,N′-tetraacetic acid (EGTA). Slides were then washed in PBS three times and stained overnight at 4°C with antibodies (see below) in

1% bovine serum in PBS. After being washed with PBS four times, samples were stained with secondary (1:1000) in 1% bovine serum albumin (BSA) in PBS for 2 h at RT. Slides were then washed four times with PBS and mounted in ProLong Gold Antifade mounting media (Life Technologies). Frozen tissue sections of WT and CDHR2 KO intestinal tissue were washed in ICB-BSA (0.5 mM $MgCl_2$, 0.2 mM EGTA, 10 mM KCl, 2 mM HEPES, pH 6.8, with 1% BSA) three times, and stained with phalloidin (1:200) for 2 h at RT. Samples were then washed with ICB-BSA two times and once with ICB without BSA and then mounted in ProLong Gold Antifade mounting media. The following dilutions were used for primary antibodies for staining: anti-villin (1:50; Santa Cruz #sc-66022), anti-SI (1:50; Santa Cruz #sc-393424), anti-DPPIV (1:200; R&D Systems #AF954), anti-ezrin (1:100; Cell Signaling Technology #3145), anti–p-ERM (1:200; Cell Signaling Technology #3726), anti-NHE3 (1:100; Novus Biologicals #NBP1-82574), anti–E-cadherin (1:500; BD Biosciences #610182), anti-USH1C (1:70; Sigma HPA027398), anti-CDHR2 (1:100; Sigma HPA012569), anti-CDHR5 (1:100; Sigma HPA009173), and anti-Myo7b (1:25; Sigma HPA039131).

Light microscopy

Confocal microscopy was performed using a Nikon A1 or A1R laser-scanning confocal microscope equipped with 60×/1.4 NA and 100×/1.49 NA objectives. Richardson-Lucy deconvolution of image volumes (20 iterations) was performed using Nikon Elements software. All images used for quantitative comparisons between WT and CDHR2 KO samples were prepared with equal treatment, acquired with identical parameters (e.g., pinhole diameter, detector gain), and processed in an identical manner. All measurements of dimensions and signal intensities from image data were performed using FIJI or Nikon Elements software.

Electron microscopy

All EM reagents were purchased from Electron Microscopy Sciences. To prepare samples for SEM, segments of WT and KO intestine were washed once with cold PBS supplemented with 1.2 mM $CaCl_2$ and 1 mM $MgCl_2$ (pH 7.2) and fixed overnight at 4°C with 3% glutaraldehyde in SEM buffer (0.1 M sucrose in 0.1 M Na-phosphate, pH 7.4), postfixed with 1% OsO_4 in SEM buffer on ice for 1 h, and then washed with SEM buffer. Samples were dehydrated in a graded ethanol series and then dried using hexamethyldisilazane or critical point drying. Samples were then mounted on aluminum stubs and coated with gold/palladium using a sputter coater. SEM imaging was performed using Quanta 250 Environmental-SEM operated in high vacuum mode with an accelerating voltage of 5–10 kV. FFT analysis of SEM images was performed using FIJI as described (Krey et al., 2016). To prepare samples for TEM, pieces of small intestine were fixed for 1 h in 1% formaldehyde, 2% glutaraldehyde, 0.1% tannic acid in 0.1 M PBS (pH 7.2). After extensive washes in PBS, the specimen was postfixed in 1% OsO_4 for 1 h on ice in the dark. Following extensive washes in ultrapure water, intestinal segments were en bloc stained with 0.5% uranyl acetate at 4°C overnight. Segments were dehydrated in a graded ethanol series, gradually infiltrated with Spurr's standard, and cured at 60°C for 8–12 h until blocks were firm, but not brittle. Thin sections were cut and post-stained with uranyl acetate and Sato's lead citrate. Images were collected with a Philips FEI T-12 transmission electron microscope operating at 100 kV.

Intensity analysis of apical markers

To measure levels of apical markers, paraffin sections of small intestinal tissues were stained with the probe of interest as outlined above.

Matched sets of WT and CDHR2 KO tissue sections were prepared and stained in parallel, and slides were imaged using identical confocal gain, pinhole, and laser power settings to allow for quantitative comparison of brush border fluorescence levels. Fluorescence intensity measurements in the brush border were made using the linescan tool in FIJI. Briefly, a line three pixels in width was drawn as to bisect the brush borders of three adjacent cells in the distal one-third of a villus (i.e., orthogonal to the microvillar axis but parallel to the crypt-villus axis), and the average signal intensity along the line was measured. Measurements were made from multiple villi ($n = 20$ for most probes), from multiple sections ($n = 4–5$ for most probes) prepared from at least two different animals.

Statistical testing

All graphs were generated and statistical analyses performed using Prism (v.7; GraphPad). For statistical testing, we used unpaired parametric t tests for distributions that satisfied the normality and equal variance assumptions. Welch's correction was used in cases where data sets did not exhibit equal variance. Nonparametric t tests were used in cases where data failed to exhibit normality. The number of measurements and level of significance are indicated in the figure legends.

REFERENCES

Adato A, Michel V, Kikkawa Y, Reiners J, Alagramam KN, Weil D, Yonekawa H, Wolfrum U, El-Amraoui A, Petit C (2005). Interactions in the network of Usher syndrome type 1 proteins. Hum Mol Genet 14, 347–356.

Ahmed ZM, Goodyear R, Riazuddin S, Lagziel A, Legan PK, Behra M, Burgess SM, Lilley KS, Wilcox ER, Riazuddin S, et al. (2006). The tip-link antigen, a protein associated with the transduction complex of sensory hair cells, is protocadherin-15. J Neurosci 26, 7022–7034.

Bahloul A, Michel V, Hardelin JP, Nouaille S, Hoos S, Houdusse A, England P, Petit C (2010). Cadherin-23, myosin VIIa and harmonin, encoded by Usher syndrome type I genes, form a ternary complex and interact with membrane phospholipids. Hum Mol Genet 19, 3557–3565.

Berg JS, Cheney RE (2002). Myosin-X is an unconventional myosin that undergoes intrafilopodial motility. Nat Cell Biol 4, 246–250.

Bitner-Glindzicz M, Lindley KJ, Rutland P, Blaydon D, Smith VV, Milla PJ, Hussain K, Furth-Lavi J, Cosgrove KE, Shepherd RM, et al. (2000). A recessive contiguous gene deletion causing infantile hyperinsulinism, enteropathy and deafness identifies the Usher type 1C gene. Nat Genet 26, 56–60.

Boeda B, El-Amraoui A, Bahloul A, Goodyear R, Daviet L, Blanchard S, Perfettini I, Fath KR, Shorte S, Reiners J, et al. (2002). Myosin VIIa, harmonin and cadherin 23, three Usher I gene products that cooperate to shape the sensory hair cell bundle. EMBO J 21, 6689–6699.

Bohil AB, Robertson BW, Cheney RE (2006). Myosin-X is a molecular motor that functions in filopodia formation. Proc Natl Acad Sci USA 103, 12411–12416.

Crawley SW, Mooseker MS, Tyska MJ (2014a). Shaping the intestinal brush border. J Cell Biol 207, 441–451.

Crawley SW, Shifrin DA Jr, Grega-Larson NE, McConnell RE, Benesh AE, Mao S, Zheng Y, Zheng QY, Nam KT, Millis BA, et al. (2014b). Intestinal brush border assembly driven by protocadherin-based intermicrovillar adhesion. Cell 157, 433–446.

Delacour D, Salomon J, Robine S, Louvard D (2016). Plasticity of the brush border—the yin and yang of intestinal homeostasis. Nat Rev Gastroenterol Hepatol 13, 161–174.

Di Palma F, Holme RH, Bryda EC, Belyantseva IA, Pellegrino R, Kachar B, Steel KP, Noben-Trauth K (2001). Mutations in Cdh23, encoding a new type of cadherin, cause stereocilia disorganization in waltzer, the mouse model for Usher syndrome type 1D. Nat Genet 27, 103–107.

el Marjou F, Janssen KP, Chang BH, Li M, Hindie V, Chan L, Louvard D, Chambon P, Metzger D, Robine S (2004). Tissue-specific and inducible Cre-mediated recombination in the gut epithelium. Genesis 39, 186–193.

Friedel RH, Seisenberger C, Kaloff C, Wurst W (2007). EUCOMM—the European Conditional Mouse Mutagenesis program. Brief Funct Genomic Proteomic 6, 180–185.

Grati M, Kachar B (2011). Myosin VIIa and sans localization at stereocilia upper tip-link density implicates these Usher syndrome proteins in mechanotransduction. Proc Natl Acad Sci USA 108, 11476–11481.

Holme RH, Steel KP (2002). Stereocilia defects in waltzer (Cdh23), shaker1 (Myo7a), and double waltzer/shaker1 mutant mice. Hear Res 169, 13–23.

In J, Foulke-Abel J, Zachos NC, Hansen AM, Kaper JB, Bernstein HD, Halushka M, Blutt S, Estes MK, Donowitz M, Kovbasnjuk O (2016). Enterohemorrhagic Escherichia coli reduce mucus and intermicrovillar bridges in human stem cell-derived colonoids. Cell Mol Gastroenterol Hepatol 2, 48–62 e43.

Kazmierczak P, Sakaguchi H, Tokita J, Wilson-Kubalek EM, Milligan RA, Muller U, Kachar B (2007). Cadherin 23 and protocadherin 15 interact to form tip-link filaments in sensory hair cells. Nature 449, 87–91.

Krey JF, Krystofiak ES, Dumont RA, Vijayakumar S, Choi D, Rivero F, Kachar B, Jones SM, Barr-Gillespie PG (2016). Plastin 1 widens stereocilia by transforming actin filament packing from hexagonal to liquid. J Cell Biol 215, 467–482.

Lefevre G, Michel V, Weil D, Lepelletier L, Bizard E, Wolfrum U, Hardelin JP, Petit C (2008). A core cochlear phenotype in USH1 mouse mutants implicates fibrous links of the hair bundle in its cohesion, orientation and differential growth. Development 135, 1427–1437.

Lentz J, Keats BJB (1993). Usher Syndrome Type I. In: GeneReviews(R), ed. RA Pagon, MP Adam, HH Ardinger, SE Wallace, A Amemiya, LJH Bean, TD Bird, CT Fong, HC Mefford, RJH Smith, and K Stephens, Seattle: University of Washington.

Li J, He Y, Lu Q, Zhang M (2016). Mechanistic basis of organization of the harmonin/USH1C-mediated brush border microvilli tip-link complex. Dev Cell 36, 179–189.

Li J, He Y, Weck ML, Lu Q, Tyska MJ, Zhang M (2017). Structure of Myo7b/USH1C complex suggests a general PDZ domain binding mode by MyTH4-FERM myosins. Proc Natl Acad Sci USA 114, E3776–E3785.

McConnell RE, Benesh AE, Mao S, Tabb DL, Tyska MJ (2011). Proteomic analysis of the enterocyte brush border. Am J Physiol Gastrointest Liver Physiol 300, G914–G926.

Okazaki N, Takahashi N, Kojima S, Masuho Y, Koga H (2002). Protocadherin LKC, a new candidate for a tumor suppressor of colon and liver cancers, its association with contact inhibition of cell proliferation. Carcinogenesis 23, 1139–1148.

Ose R, Oharaa O, Nagase T (2012). Galectin-1 and galectin-3 mediate protocadherin-24-dependent membrane localization of β-catenin in colon cancer cell line HCT116. Curr Chem Genomics 6, 18–26.

Ose R, Yanagawa T, Ikeda S, Ohara O, Koga H (2009). PCDH24-induced contact inhibition involves downregulation of β-catenin signaling. Mol Oncol 3, 54–66.

Pan B, Akyuz N, Liu XP, Asai Y, Nist-Lund C, Kurima K, Derfler BH, Gyorgy B, Limapichat W, Walujkar S, et al. (2018). TMC1 forms the pore of mechanosensory transduction channels in vertebrate inner ear hair cells. Neuron 99, 736–753 e736.

Pan L, Yan J, Wu L, Zhang M (2009). Assembling stable hair cell tip link complex via multidentate interactions between harmonin and cadherin 23. Proc Natl Acad Sci USA 106, 5575–5580.

Pawlowski KS, Kikkawa YS, Wright CG, Alagramam KN (2006). Progression of inner ear pathology in Ames waltzer mice and the role of protocadherin 15 in hair cell development. J Assoc Res Otolaryngol 7, 83–94.

Pena JF, Alie A, Richter DJ, Wang L, Funayama N, Nichols SA (2016). Conserved expression of vertebrate microvillar gene homologs in choanocytes of freshwater sponges. EvoDevo 7, 13.

Petersen KJ, Goodson HV, Arthur AL, Luxton GW, Houdusse A, Titus MA (2016). MyTH4-FERM myosins have an ancient and conserved role in filopod formation. Proc Natl Acad Sci USA 113, E8059–E8068.

Schwander M, Kachar B, Muller U (2010). The cell biology of hearing. J Cell Biol 190, 9–20.

Senften M, Schwander M, Kazmierczak P, Lillo C, Shin JB, Hasson T, Geleoc GS, Gillespie PG, Williams D, Holt JR, Muller U (2006). Physical and functional interaction between protocadherin 15 and myosin VIIa in mechanosensory hair cells. J Neurosci 26, 2060–2071.

Siemens J, Kazmierczak P, Reynolds A, Sticker M, Littlewood-Evans A, Muller U (2002). The Usher syndrome proteins cadherin 23 and harmonin form a complex by means of PDZ-domain interactions. Proc Natl Acad Sci USA 99, 14946–14951.

Siemens J, Lillo C, Dumont RA, Reynolds A, Williams DS, Gillespie PG, Muller U (2004). Cadherin 23 is a component of the tip link in hair-cell stereocilia. Nature 428, 950–955.

Sundberg U, Obrink B (2002). CEACAM1 isoforms with different cytoplasmic domains show different localization, organization and adhesive properties in polarized epithelial cells. J Cell Sci 115, 1273–1284.

Tokuo H, Ikebe M (2004). Myosin X transports Mena/VASP to the tip of filopodia. Biochem Biophys Res Commun 319, 214–220.

Tuxworth RI, Weber I, Wessels D, Addicks GC, Soll DR, Gerisch G, Titus MA (2001). A role for myosin VII in dynamic cell adhesion. Curr Biol 11, 318–329.

VanDussen KL, Stojmirovic A, Li K, Liu TC, Kimes PK, Muegge BD, Simpson KF, Ciorba MA, Perrigoue JG, Friedman JR, et al. (2018). Abnormal small intestinal epithelial microvilli in patients with Crohn's disease. Gastroenterology 155, 815–828.

Verpy E, Leibovici M, Zwaenepoel I, Liu XZ, Gal A, Salem N, Mansour A, Blanchard S, Kobayashi I, Keats BJ, et al. (2000). A defect in harmonin, a PDZ domain-containing protein expressed in the inner ear sensory hair cells, underlies Usher syndrome type 1C. Nat Genet 26, 51–55.

Weck ML, Crawley SW, Stone CR, Tyska MJ (2016). Myosin-7b promotes distal tip localization of the intermicrovillar adhesion complex. Curr Biol 26, 2717–2728.

Weil D, El-Amraoui A, Masmoudi S, Mustapha M, Kikkawa Y, Laine S, Delmaghani S, Adato A, Nadifi S, Zina ZB, et al. (2003). Usher syndrome type I G (USH1G) is caused by mutations in the gene encoding SANS, a protein that associates with the USH1C protein, harmonin. Hum Mol Genet 12, 463–471.

Yan J, Pan L, Chen X, Wu L, Zhang M (2010). The structure of the harmonin/sans complex reveals an unexpected interaction mode of the two Usher syndrome proteins. Proc Natl Acad Sci USA 107, 4040–4045.

Yu IM, Planelles-Herrero VJ, Sourigues Y, Moussaoui D, Sirkia H, Kikuti C, Stroebel D, Titus MA, Houdusse A (2017). Myosin 7 and its adaptors link cadherins to actin. Nat Commun 8, 15864.

Zhang H, Berg JS, Li Z, Wang Y, Lang P, Sousa AD, Bhaskar A, Cheney RE, Stromblad S (2004). Myosin-X provides a motor-based link between integrins and the cytoskeleton. Nat Cell Biol 6, 523–531.

Zihni C, Munro PMG, Elbediwy A, Keep NH, Terry SJ, Harris J, Balda MS, Matter K (2014). Dbl3 drives Cdc42 signaling at the apical margin to regulate junction position and apical differentiation. J Cell Biol 204, 111–127.